Journal of Magnetic Resonance 305 (2019) 195–208

Contents lists available at ScienceDirect

Journal of Magnetic Resonance

journal homepage: www.elsevier.com/locate/jmr

Design of a novel antisymmetric coil array for parallel transmit cardiac MRI in pigs at 7 T ☆

Ibrahim A. Elabyad [a,b,*], M. Terekhov [a], M.R. Stefanescu [a], D. Lohr [a], M. Fischer [a], L.M. Schreiber [a]

[a] Chair of Cellular and Molecular Imaging, Comprehensive Heart Failure Center (CHFC), University Hospital Wuerzburg, D-97078 Wuerzburg, Germany
[b] Department of Electronics and Communications Engineering, Thebes Higher Institute of Engineering, Cairo, Egypt

ARTICLE INFO

Article history:
Received 8 May 2019
Revised 12 June 2019
Accepted 4 July 2019
Available online 5 July 2019

Keywords:
Cardiac MRI
Ex-vivo pigs
Multichannel coil arrays
UHF
RF shimming
Parallel transmit (pTx)

ABSTRACT

The design, simulation, assembly and testing of a novel dedicated antisymmetric transmit/receive (Tx/Rx) coil array to demonstrate the feasibility of cardiac magnetic resonance imaging (cMRI) in pigs at 7 T was described. The novel antisymmetric array is composed of eight elements based on mirrored and reversed loop orientations to generate varying B_1^+ field harmonics for RF shimming. The central four loop elements formed together a pair of antisymmetric L-shaped channels to allow good decoupling between all neighboring elements of the entire array. The antisymmetric array was compared to a standard symmetric rectilinear loop array with an identical housing dimension. Both arrays were driven in the parallel transmit (pTx) mode forming an 8-channel transmit and 16-channel receive (8Tx/16Rx) coil array, where the same posterior array was combined with both anterior arrays. The hardware and imaging performance of the dedicated cardiac arrays were validated and compared by means of electromagnetic (EM) simulations, bench-top measurements, phantom, and *ex-vivo* MRI experiments with 46 kg female pig. Combined signal-to-noise ratio (SNR), geometry factor (g-factor), noise correlation maps, and high resolution *ex-vivo* cardiac images were acquired with an in-plane resolution of 0.3 mm × 0.3 mm using both arrays. The novel antisymmetric array enhanced the SNR within the heart by about two times and demonstrated good decoupling and improved control of the B_1^+ field distributions for RF shimming compared to the standard coil array. Parallel imaging with acceleration factor (R) up to 4 was possible using the novel antisymmetric coil array while maintaining the mean g-factor within the heart region of 1.13.

1. Introduction

Design of radiofrequency (RF) coil arrays for ultrahigh field (UHF) ($B_0 \geq 7\,\mathrm{T}$) magnetic resonance imaging (MRI) yields an improvement of the signal-to-noise ratio (SNR) compared to lower field strength ($\leq 3\,\mathrm{T}$) [1,2]. Moreover, due to the reduced wavelength effects, which arise at 7 T ($\lambda_{\mathrm{eff}} \approx 12\,\mathrm{cm}$), constructive and destructive interferences of the transmitted B_1^+ field magnitude and hence strong corresponding intensity artifacts will occur in the acquired MR images [3–6]. To solve the issues of the B_1^+ field inhomogeneity for brain imaging at 7 T, different coil array designs, concepts, and hardware technologies have been introduced [7–21].

Cardiac magnetic resonance imaging (cMRI) is promising for clinical applications due to the possibility to differentiate various myocardial diseases at 7 T. However, unlike in the brain, cMRI at 7 T is considered to be a challenge. On one hand there is the necessity to optimize a large number of resonant elements in order to enhance the penetration of B_1^+ field within the thorax (about 10 cm from the coil surface to the heart), to improve the B_1^+ field uniformity, maximize the SNR, and maximize the transmission efficiency within the heart. On the other hand the specific absorption rate (SAR) needs to be kept within the standard limits according to IEC or national regulations. Therefore, different coil arrays and design concepts have been introduced for cMRI in humans at UHF including, transmission line resonators [22,23], multichannel Tx/Rx loop arrays [24–30], dipole antenna arrays [31–37], combined dipoles and loops arrays [38,39] and dielectric resonant antenna arrays [40].

An optimized multichannel transceiver array composed of independent coil elements (typically 8 to 32) lead to reduced inhomogeneity of the transmit B_1^+ field. By optimizing the magnitude and phase of each individual transmit coil element, the combined B_1^+ field can be shaped and controlled in order to achieve better B_1^+ field homogeneity within the targeted Region-Of-Interest (ROI),

---

☆ This project is funded by the German Ministry of Education and Research (BMBF) with grant # 01EO1004 & 01EO1504.

* Corresponding author.
E-mail addresses: Elabyad_I@ukw.de (I.A. Elabyad), Terekhov_M@ukw.de (M. Terekhov), stefanescu.m.roxana@gmail.com (M.R. Stefanescu), E_Lohr_D@ukw.de (D. Lohr), mofi94@yahoo.de (M. Fischer), Schreiber_L@ukw.de (L.M. Schreiber).

https://doi.org/10.1016/j.jmr.2019.07.004
1090-7807/

which here is the heart. This process called RF shimming or B_1^+ shimming [41–46] and can be applied via software using the pTx system available at the modern 7 T scanners without modifying the coil hardware. To effectively use RF shimming, the outcome transmit B_1^+ field arrangement of the individual coil elements should reveal spatially separated profiles in the required ROI.

Although, increasing the number of elements in the array enhances the signal-to-noise ratio (SNR), allows accelerations with lower noise amplification g-factor for parallel imaging, and improves the B_1^+ field homogeneity, the coupling between neighboring loops will increase, and the RF shimming will get less efficient. Therefore, novel coil array designs with different coil geometries (e.g. antisymmetric configuration), with combination of different loop shapes (e.g. circular, rectangular, octagonal, or triangular) and with novel decoupling mechanisms and element distributions are required for RF shimming. A recent study presented a dedicated multichannel symmetric Tx/Rx coil array for cMRI in pigs at 7 T [47]. A significant degradation of the SNR and the B_1^+ field homogeneity was shown by using a human coil array for performing cMRI in pigs compared to a dedicated array for pigs. Cardiac coil arrays based on multichannel Tx/Rx loops with optimal coil dimensions, geometry, and decoupling schemes enable RF shimming and therefore give control over the transmit B_1^+ field homogeneity within the heart region.

In this paper, a novel antisymmetric transceiver pTx coil array was designed and evaluated for cMRI in pigs at 7 T. The novel antisymmetric array was compared to the rectilinear coil array. Both arrays were characterized through bench-top measurements, EM-simulations, phantom and *ex-vivo* pig measurements using the pTx system of the 7 T Siemens Scanner. High resolution *ex-vivo* images were acquired with an in-plane resolution of up to 0.3 mm × 0.3 mm using both arrays. Two fold higher SNR was achieved using the antisymmetric array compared to the rectilinear array.

2. Materials and methods

2.1. The symmetric rectilinear coil array (Design 1)

The anterior array for Design 1 was composed of eight elements and was designed using the standard 4 × 2 rectangular symmetric elements distribution. The optimal size of the loop elements for the anterior array was selected to be 4 cm × 8 cm as recently described in [47]. For the anterior array, all central elements 2, 3, 4, 5, 6 and 8 have the same symmetric dimensions as shown in Fig. 1a. However, elements 1 and 7 were adjusted to keep some free space on the housing by taking into considerations the legs of the pig. An effective surface area of 64 cm^2 was optimized for each pair of the elements (e.g., the combination of elements 1 and 2 in one Tx channel) with a channel pair size of 4 cm × 16 cm. Two tuning capacitors (C_1^t and C_2^t) were distributed equally in the gaps between the segment for each resonant loop in order to have the element resonating at 297.2 MHz. The decoupling of the adjacent coil elements (e.g., element 1 and 2) was accomplished using a common conductor and a shared decoupling capacitor (SDC) of (C_1^d)[48]. For all neighboring elements (e.g., element 1 and 3), the decoupling was accomplished using two equal capacitors (C_3^d) in addition to a horizontal decoupling gap of 1.8 cm. The external dimension for the anterior array of Design 1 was 17.2 cm × 24.6 cm.

2.2. The novel antisymmetric anterior coil array (Design 2)

The novel antisymmetric anterior coil array of Design 2 was composed of eight elements based on mirrored and reversed loop orientations. Six elements (3, 4, 5, 6, 7 and 8) were distributed around the central two elements (1 and 2) in mirrored and reversed loop configurations as shown in Fig. 1c. The central four loop elements formed together a pair of antisymmetric L-shaped channels to allow good decoupling between all neighboring elements of the entire array. This method allows generating varying B_1^+ field harmonics for each individual Tx channel for RF shimming. The size of the central two elements 1 and 2 was 3.50 cm × 7.35 cm. For both central elements 1 and 2, three tuning capacitors (C_1^t) were distributed in the gaps between the segment for each resonant loop in order to have the element resonating at 297.2 MHz. Their respective locations were chosen to allow capacitive decoupling with the neighboring elements. The decoupling between the central elements was accomplished using a SDC of (C_1^d). The elements 3 and 4 were reversed and decoupled with elements 1 and 2 using a SDC of (C_2^d). The elements 5 and 7 and the reversed identical elements 6 and 8 were decoupled using a SDC of (C_3^d). The central elements 1 and 2 were decoupled from the neighboring elements 5, 6, 7 and 8 using capacitive decoupling (C_6^d and C_7^d) in addition to a decoupling gap of 1.5 cm. The external dimension for the array was 15.9 cm × 23.6 cm.

2.3. The posterior array

The posterior array was built using 4 × 2 rectangular symmetric elements configuration as shown in Fig. 1b with element dimensions (5.0 cm × 10 cm) [47].

In order to maintain the same imaging position and not moving the phantoms or the pig between scans, both anterior arrays (i.e., the standard rectilinear array of Fig. 1d and the novel antisymmetric array of Fig. 1f were combined with the same posterior array of Fig. 1e.

2.4. Channel pairing for the pTx system

The 7 T Magnetom Terra scanners are equipped with only eight transmit channels (8Tx). Therefore, for all arrays, each two elements were combined in one Tx channel forming four independent Tx channels for the anterior array and another four independent Tx channels for the posterior array (8Tx/16Rx). Since Design 1 is symmetric, each two elements, which have a common conductor and a SDC (e.g., elements 7 and 8) were combined in one Tx channel (T_{x1}). The same for the other channels T_{x2}, T_{x3} and T_{x4} as described in Table 1. The other four *Tx* channels were set for the posterior array of Fig. 1b (T_{x5}, T_{x6}, T_{x7} and T_{x8}) [47]. However, for the antisymmetric array of Fig. 1c, the selection of the channel paring was composed of two central antisymmetric L-shaped channels (T_{x2} and T_{x3}) and two antisymmetric channels (T_{x1} and T_{x4}) as described in Table 1. Each array was connected to a Tx/Rx switch interface via two plugs (ODU GmbH & Co. KG, Mühldorf a. Inn, Germany).

2.5. EM simulations of the dedicated coil arrays

For coil design and B_1^+ field optimizations, comprehensive EM simulations were performed using CST® Microwave Studio (Computer Simulation Technology AG Darmstadt, Germany) for both arrays at 297.2 MHz. Fig. 1g shows the RF simulation model of the dedicated cardiac coil arrays developed for a 50 kg pig. Each cardiac array consists of eight elements for the anterior and eight elements for the posterior sections.

All coil arrays were loaded with two different phantom loads to test worst and best cases of the cardiac arrays performance since pigs have a significant heterogeneity of the thorax structure. The

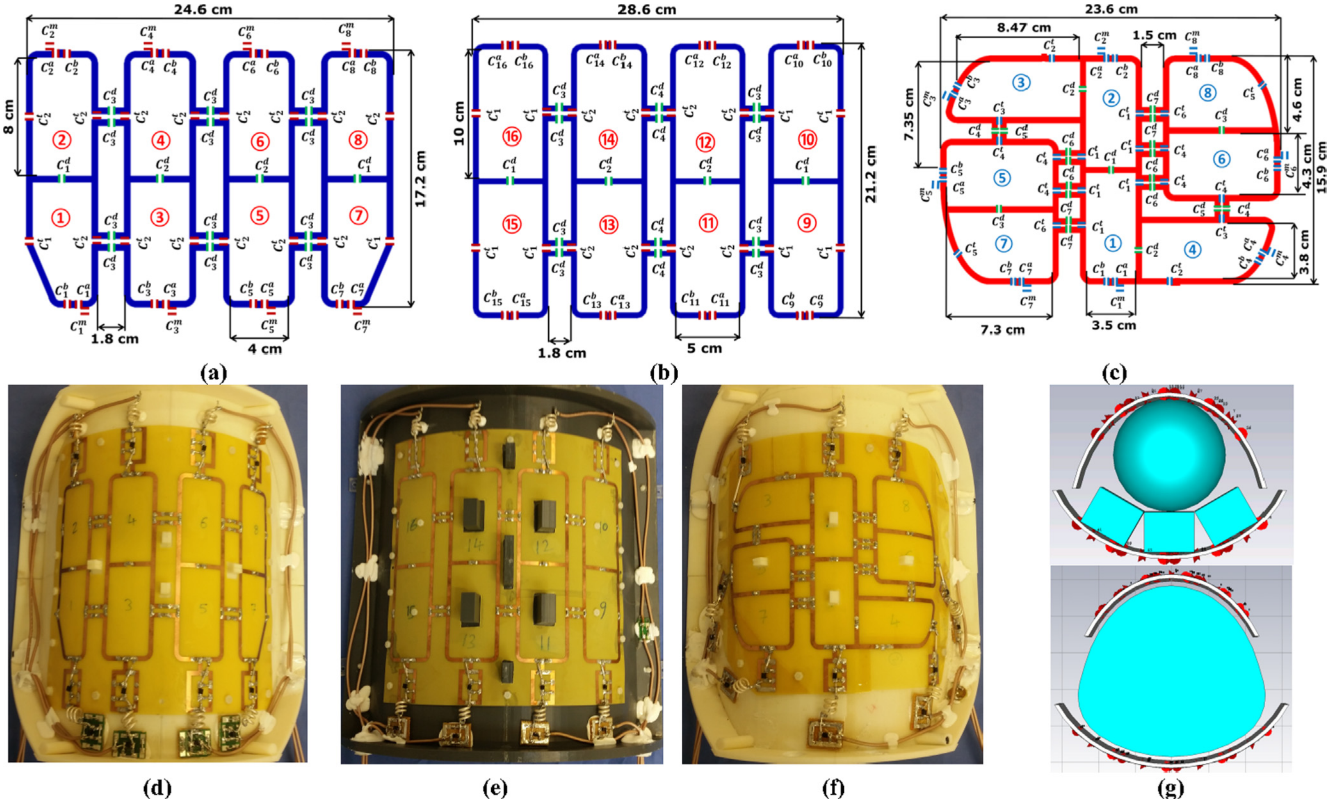

Fig. 1. Schematics and prototypes of the dedicated pig coil arrays including the element dimensions, the capacitor variables, and the element numbers. The anterior array of Design 1 (a) & (d), posterior array of Design 1 (b) & (e), anterior array of Design 2 (c) & (f). (g) Simulation models of a dedicated pig cardiac array loaded with a 16 cm diameter spherical phantom combined with six bottles (top) [47] and with a pig body phantom (bottom). Note: in all schematics, the variable names for capacitors are: *m* for matching, *t* for tuning, *d* for decoupling and *a*, *b* for splitting tuning at the feeding ports. Both anterior arrays were combined with the same rectilinear posterior array of Fig. 1e [47]. Obtained permission from IEEE to include Fig. 2(b) and e from ref. [47] (License Number: 4606371380227)

Table 1
Measured relative phases and loaded to unloaded quality factor (Q_{lo}/Q_{un}) ratios for both anterior arrays of Design 1 and Design 2 loaded with an *ex-vivo* pig of 46 kg.

Channel #	Element #	Phase [°]	Q_{lo}/Q_{un}	Ratio
Anterior Array of Design 1 (Fig. 1a)				
T_{x1}	7	58	32/45	0.71
	8	60	32/42	0.76
T_{x2}	5	45	30/40	0.75
	6	47	31/40	0.77
T_{x3}	3	31	30/40	0.75
	4	32	29/40	0.72
T_{x4}	1	52	32/45	0.71
	2	64	32/42	0.76
Anterior Array of Design 2 (Fig. 1c)				
T_{x1}	6	60	28/37	0.76
	8	72	44/70	0.63
T_{x2}	1	41	68/90	0.75
	4	46	36/56	0.64
T_{x3}	2	50	68/90	0.75
	3	66	38/56	0.68
T_{x4}	5	102	28/37	0.76
	7	100	44/70	0.63

first phantom load consisting of a 16 cm diameter spherical phantom combined with another six bottles (Dimensions: 7.0 × 5.6 × 14 cm^3) [47]. The second phantom load was a pig body phantom mimicking the shape of a pig with width, height and length of 25, 23 and 20 cm, respectively, as shown in Fig. 1g, bottom. This load was used only for simulations and B_1^+ shimming. Both phantoms have the same electrical properties with ($\varepsilon_r = 59.3$, $\sigma = 0.79$ S/m). All feeding ports, tuning, matching, and decoupling capacitors were modeled as 50 Ω discrete face ports for RF circuit co-simulations [49]. After adjusting the meshing for all coils, the final total number of mesh cells was 25.3 and 27.3 million for Design 1 and 2, respectively. Individual 16-AC simulation tasks corresponding to the 16 elements for each array combination were evaluated at 297.2 MHz. The 3D-data of the H-field for each resonance element was exported to MATLAB® (MathWorks, Natick, MA, USA) for post-processing and B_1^+ phase shimming.

All coil arrays were designed to have a copper (Cu) track width of 4 mm and a thickness of 35 µm etched on a 0.3 mm FR4 ($\varepsilon_r = 4.24$ and tan$\delta = 0.014$ at 297.2 MHz) printed circuit board (PCB) (Q-print Electronic GmbH, Heddesheim, Germany). To increase the filling factor and improve the SNR, all flexible PCBs were bent around a semi-half elliptical shape housing of 5 mm thickness made from ABS$^+$ material ($\varepsilon_r = 2.8$ and tan$\delta = 0.0095$ at 297.2 MHz) and were fixed using screws and nuts. Fixed chip non-magnetic capacitors (Voltronics Corp., Denville, NJ, USA) were used for tuning, matching and decoupling.

2.6. Characterization of the cardiac arrays

2.6.1. Measurements of the scattering parameters

Both arrays were optimized (i.e., matching, tuning and decoupling capacitors) on bench using the cadaver of 46 kg pig as the load. The scattering parameters (S-matrix) for both arrays were measured using an E5080A 4-port Vector Network Analyzer (VNA) (Keysight Technologies, Santa Rosa, CA, USA). The measured and simulated S-matrix for the first phantom load (a 16 cm spherical phantom combined with six bottles), which represents the worst case of loading are shown in the Appendix (Tables 2 and 3). For the pig body phantom we show only the simulated S-matrix (Tables 4 and 5). For each resonant element, one cable trap was designed to remove the unbalanced surface current and cable resonance on the coaxial cables. The initially optimized capacitors values using CST RF-circuit co-simulation were in good agreement with the optimized values on bench-top measurements (Tables 6 and 7). The prototypes of the dedicated cardiac coil arrays were shown in Fig. 1d–f.

2.6.2. Measurements of the phase shifts

To adjust the phase shift between elements, individual low pass pi-network discrete phase shifter (PS) circuits consists of two equal capacitors and one nonmagnetic and high quality factor inductor (Coilcraft, Inc., Silver Lake Road, Cary, IL) were designed for each element. The PS was inserted between the resonant element and the cable trap. For both array designs, the implemented hardware phases were obtained using an in-house developed MATLAB script as described in [46,47]. The measured absolute hardware phases for all anterior channels were described in Table 1. For the elements 9–16 of the same posterior array, the phases were measured as 100°, 82°, 72°, 64°, 73°, 72°, 96°, and 92°, respectively.

2.7. MR measurements

All MR measurements were performed on a 7 T whole-body MAGNETOM Terra scanner (Siemens Healthcare, Erlangen, Germany) equipped with a 16 kW RF power amplifier for eight channel pTx mode. For all MR measurements (phantom validations and *ex-vivo*), the same rectilinear posterior array of Fig. 1e [47] was combined with both anterior arrays of Design 1 and of Design 2. Phantoms and the *ex-vivo* pig were not moved between scans in order to maintain the same imaging position. Both coils were fed with the same reference voltage.

2.7.1. Phantom MR measurements

A phantom MR experiment was performed using the phantom setup of Fig. 1g (top) (a 16 cm spherical phantom combined with the 6 bottles). The measurements of the B_1^+ spatial distribution in both phantoms and *ex-vivo* experiments were performed using mapping of magnetization FA by the saturated double flip angle (SDAM) approach based on a GRE sequence. The GRE-SDAM measurement parameters were: TE/TR 1.8/4000 ms, pixel resolution 2 × 2 mm, slice thickness 3.5 mm, and number of slices 36. The FA maps were acquired in two successive measurements with 30° respective 60°. The actual FA maps were reconstructed using an in-house developed MATLAB script.

2.7.2. Ex-vivo MR measurements

Both coil arrays were tested in an *ex-vivo* experiment with one female pig (German Landrace pig, 46 kg in weight obtained from Heinrichs Tierzucht GmbH, Heinsberg, Germany). The animal was provided for *ex-vivo* measurements, following its approved use in project 55.2 DMS 2532-2-664 (Regierung Unterfranken, Germany). Euthanasia was performed with an intravenous application of 150 mg/kg pentobarbital under isoflurane anesthesia with fentanyl analgesia. The MR measurements were performed starting with Design 1 followed by Design 2 while keeping the posterior array of Fig. 1b the same without moving the animal between scans. The pig was placed head first in supine position inside the scanner. The initial coil position was marked to be in the same place after exchanging between both anterior arrays. The position of the heart was estimated to fit approximately in the center of the coil.

The sequence parameters for CINE short axis (SA) views were: TR/TE = 69.52/4.07, FA = 45°, pixel size = 0.3 × 0.3 mm, GRAPPA acceleration factor R = 2, number of averages = 8, FOV = 320 × 320 and a slice thickness of 4 mm. The total measurement time was about four hours covering the preparatory pulse sequences, anatomical CINE GRE sequence, FA maps, SNR maps, noise correlation, and the g-factor maps.

2.8. Outlook of B_1^+ shimming for the coil arrays

2.8.1. Decorrelation analysis of the Tx-Channels B_1^+ maps

In order to characterize and compare between the pTx B_1^+ adjustments capabilities for RF shimming of both designs, the B_1^+ maps of the combined pTx RF channels were additionally analyzed in order to reveal the effective amount of degrees of freedom available for B_1^+ shimming procedure. For this purpose, the so-called, "multiband decorrelation-stretch" procedure was applied to the four channels of the anterior array part for each design individually. This procedure was based on the principal component analysis (PCA) of the channel maps, which was widely used to reveal correlations and subsequent "compression" of the correlated physical array channels to the smaller amount of de-correlated virtual eigen-channels. The numerous applications of PCA-based coil compression approaches can be found in [50]. We therefore, only provide a brief description of the analysis algorithm. The decorrelation-stretch procedure consists of the following steps: (1) selecting the coronal plane slice in the numerical body phantom B_1^+ maps and forming L × M × N array, where L × M was the dimensions of the B_1^+ map coronal slice and N was the number of bands (pTx channels); (2) whitening of the channels, subtracting mean and normalizing to standard deviation; (3) rotating the bands into the eigen-space of the correlation matrix using singular value decomposition (SVD); (4) apply a stretch according to the found singular components in the eigen-space, leaving channel maps de-correlated and normalized in the eigen-space; (5) rotate back to the original band-space, where the channels remain de-correlated and normalized; and (6) restore a mean in each channel. The difference found in the normalized original and de-correlated stretched B_1^+ maps will reveal the strength of correlation presented in the original physical channels.

2.8.2. Static B_1^+ shimming

For a specific RF-pulse waveform and constant driving amplitudes delivered by radio frequency power amplifier (RFPA), the spatial distribution of combined B_1^+field produced by N Tx-channels can be represented as sum of individual array elements spatial profiles $\mathrm{b}_{1\mathrm{k}}^+(\mathrm{r})$ weighted by phasors of driving currents applied with phase shifts Φ_k.

$$B_1^+(\mathrm{r}) = \left|\sum\nolimits_{\mathrm{k}=0}^{\mathrm{N}} \Phi_\mathrm{k} \mathrm{b}_{1\mathrm{k}}^+(\mathrm{r})\right|, \tag{1}$$

where $\Phi_k = e^{i\phi_k}$. The static B_1^+ shimming of the array was performed by control of the phasor vector $\{\Phi\} = \{\Phi_1 \cdots \Phi_\mathrm{N}\}$ to achieve the targeted spatial homogeneity of the combined B_1^+field. The task can be solved numerically as an optimization problem for the cost function F_{opt} maximizing the combined $B_1^+(r)$ field homogeneity and total arrays transmit efficiency within the selected region $\Delta\mathrm{r}$.

$$\Phi = \mathrm{argmax}_{\Phi\in\mathrm{C}}\left(F_{opt}(\Delta\mathrm{r})\right) \tag{2}$$

The geometry of the designed thorax arrays creates intrinsically strong gradients of theB_1^+field in anterior-posterior direction leading to insufficient FA value in the dorsal regions of the myocardial wall. This put higher demand on the uniformity of B_1^+field to be achieved with default static phases shimming. Therefore, in order to find the phasor forming the optimal combined B_1^+field we have introduced the cost function with additionally enhanced sensitivity to homogeneity within a specific optimization region $\Delta\mathrm{r}$ as

$$F_{opt}(\Delta\mathrm{r}) = \frac{\mathrm{median}(B_1^+(\Delta\mathrm{r}) \cdot \sigma_\mathrm{n}^{-1}(\Delta\mathrm{r})}{[\max(B_1^+(\Delta\mathrm{r})) - \mathrm{mean}(B_1^+(\Delta\mathrm{r}))]} .\mathrm{Tx}_\mathrm{eff}(\Delta\mathrm{r}) \tag{3}$$

where $\sigma_{\mathrm{n}}(\Delta \mathrm{r}) = \frac{\mathrm{std}(B_1^+(\Delta \mathrm{r}))}{\mathrm{mean}(B_1^+(\Delta \mathrm{r}))}$ is the relative standard deviation and $\mathrm{Tx}_{\mathrm{eff}}(\Delta \mathrm{r}) = \frac{\left|\sum_{\mathrm{k}}^{\mathrm{N}} \Phi_{\mathrm{k}} \mathrm{s}_{\mathrm{k}}^+\right|}{\sum_{\mathrm{k}}^{\mathrm{N}} \left|\Phi_{\mathrm{k}} \mathrm{s}_{\mathrm{k}}^+\right|}$ is the transmitting efficiency factor. The problem (3) has a numerous locally optimal solutions if a standard approach based on the non-linear solvers was applied. All computations on the B_1^+field were performed using an in-house developed MATLAB 2017b scripts.

3. Results

3.1. Characterization of the cardiac arrays

3.1.1. S-Matrix measurements

For both arrays, the reflection coefficient S_{ii} corresponding to each coil element was measured with a 46 kg pig load to be −20 ± 7 dB. The transmission coefficient S_{ij} was measured to be below −12 and −14 dB for Design 1 and Design 2, respectively. For phantom measurements, S_{ij} was measured to be below −9 dB and −13 dB for Design 1 and Design 2, respectively. The antisymmetric coil design shows better decoupling among all neighboring loops compared to the rectilinear array as shown in Table 3.

One of the main issues of the rectilinear array design was the coupling between the diagonal elements (e.g. between elements 1 and 4 or elements 2 and 3), which was minimized in the antisymmetric design. The rectilinear array could generate magnetic coupling between adjacent elements or diagonal elements due to diagonal coupling even with a large gap distance of 1.8 cm. The arrangement of the elements in the further novel array Design 2 allows for additional shared decoupling capacitors for the central antisymmetric L-shaped elements (e.g., between element 1 and 4 or element 2 and 3) and with capacitive decoupling in addition to gaps between the other four elements 5, 6, 7 and 8. This antisymmetric array design with reversed and mirrored loops facilitated the decoupling between all elements in the entire array. Therefore, good isolations between the individual elements were obtained in order to ensure spatially unique sensitivity for all channels.

3.1.2. Measurements of the phase shifts

For Design 1, the hardware phases were adjusted to have approximately the same reference phase for each two channel formed by the combination of two elements which have a common conductor and a SDC. For example the phase shift between elements 1 and 2 was 8° and between elements 3 and 4 was 1° (Table 1). For the posterior array of Design 1, the phases were adjusted in the same way. However, for Design 2 the adjustments of the initial hardware phases and the channel pairing were found to be more complex because the structure was antisymmetric. Each two mirrored and reversed elements (e.g., elements 1 and 4) or (elements 2 and 3) were combined in one Tx channel (T_{x2} and T_{x3}), respectively. The hardware phase setting for each channel pair provides the maximum efficiency of the coil elements with spatially unique B_1^+ field profiles within a16 cm diameter spherical phantom.

3.1.3. Quality factors measurements

Since both anterior arrays of Design 1 and Design 2 have different element dimensions and bending conditions, the quality factors differed. For example, for Design 1, the elements 1, 2, 7, and 8 had stronger bending than elements 3, 4, 5 and 6 (Fig. 1a). The same was the case for Design 2: elements 3, 4, 5, 6, 7 and 8 bent more than elements 1 and 2 (Fig. 1c). For both anterior arrays of Design 1 and Design 2, the loaded Q_{lo} were measured with a 46 kg *ex-vivo* pig from the reflection coefficients (S_{ii}). The Q_{lo}/Q_{un} ratios for all elements of Design 1 were in the range of 0.71 to 0.77. The Q_{lo}/Q_{un} ratios for all elements of Design 2 were in the range of 0.63 to 0.75 as listed in Table 1. The Q_{lo}/Q_{un} ratios for the posterior array were in the range of 0.35 to 0.55 [47], which indicate that the sample noise dominates the coil noise.

3.2. Phantom MR measurements

3.2.1. Individual channel FA maps

Figs. 2 and 3 demonstrate the normalized central coronal B_1^+ field distribution within a 16 cm diameter spherical phantom for the individual four channels of the anterior arrays of Design 1 and Design 2, respectively. The normalized B_1^+ field distribution of the four individual anterior channels obtained from CST simulations was compared to the normalized FA maps obtained from DAM MR measurements. The combined B_1^+ field for each channel was normalized to its own maximum value. For Design 2, the simulated B_1^+ field and the measured FA maps for the four individual Tx channels (T_{x1}, T_{x2}, T_{x3}, and T_{x4}) were in good agreement and matched well with minima, maxima and even with the destructive interference locations (Fig. 3). However, for Design 1, there were some differences in measured B_1^+ field patterns for the two channels, T_{x3} and T_{x4} as shown in Fig. 2c, d, g and h.

3.2.2. Combined FA maps

Fig. 4 shows the simulated B_1^+ field distribution and the measured FA maps within a 16 cm diameter spherical phantom from all combined eight channels. The relative standard deviation (RSD) which was defined by the ratio of the SD of the B_1^+ field to the mean of the B_1^+ field was evaluated in the same selected ROI. It is of interest to note that the distribution of the combined B_1^+ field generated from both coils was considerably different especially with the destructive interference locations. For Design 1, the locations of the constructive interference were near to the peripheral of the phantom and the destructive interferences were much bigger in size than for Design 2. For Design 2, a constructive interference with local maximum was pronounced at the center of the phantom. The RSD values were computed in the selected ROI as 0.37 and 0.21 for both anterior arrays combined with the same posterior array. Hence, the novel antisymmetric array improved the combined B_1^+ field homogeneity by about 43% compared to the rectilinear array. Design 2 showed better homogeneity with less destructive interference combined with the same posterior array. The posterior array has about 10% contribution of the total B_1^+ field, which is why changing the posterior array has minor effects on the B_1^+ field within the heart region. This confirms that the posterior array has minimal impact at 16 cm depth.

3.3. Ex-vivo pig MR measurements

3.3.1. Noise correlation

Fig. 5 shows noise correlation matrices for an *ex-vivo* pig experiment acquired using Design 1 (left) and Design 2 (right). Despite the complexity of the novel antisymmetric design, the noise correlation was decreased by about 25% compared to the rectilinear array, which was mainly due to better decoupling between elements.

3.3.2. g-Factor maps

Parallel imaging performance was measured with acceleration factors R = 2, 3 and 4 for both dedicated arrays as shown in Fig. 6 using a vendor-provided sequence for coil tests on the scanner (coil utils, Siemens Healthcare, Germany). The mean ± SD of measured g-factor maps from within the heart region for an *ex-vivo* pig experiment with acceleration from the left-right (L/R) direction

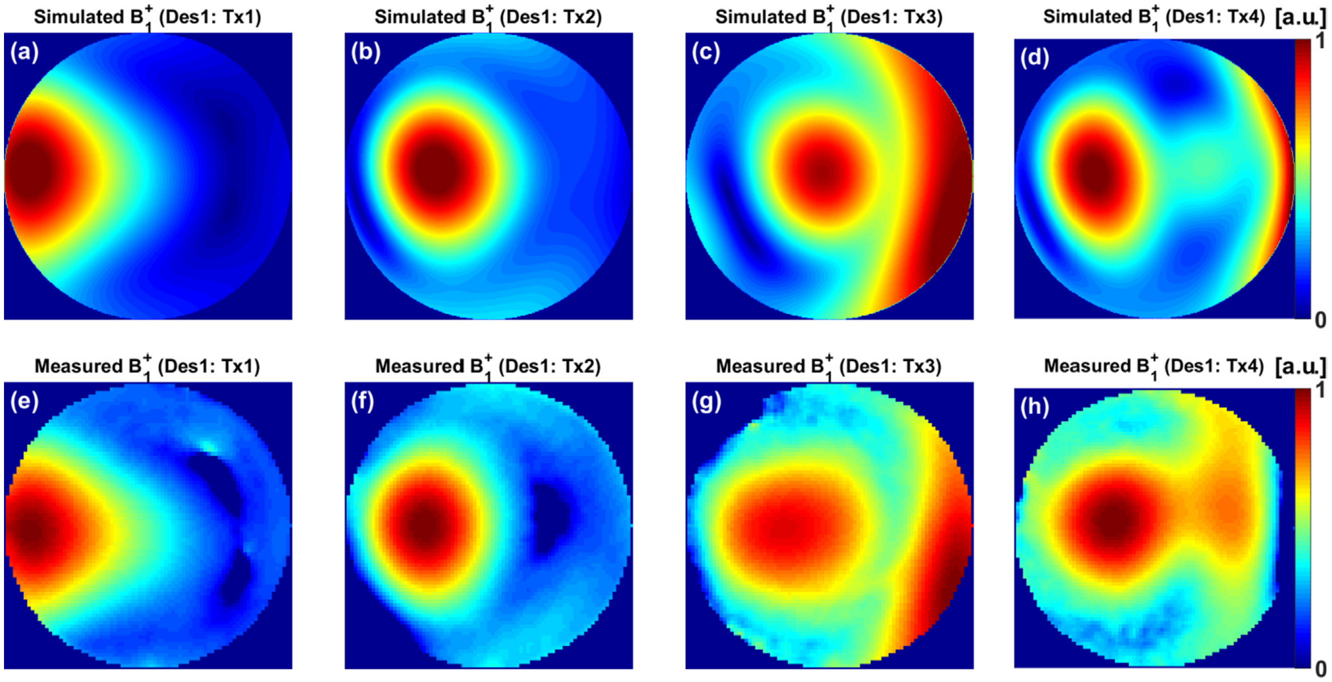

Fig. 2. Simulated and measured normalized central coronal B_1^+ field distributions for the individual four channels: T_{x1},T_{x2},T_{x3}, andT_{x4} of the anterior array of Design 1 within a 16 cm diameter spherical phantom. Simulation (a)–(d). Measurement (e)–(h).

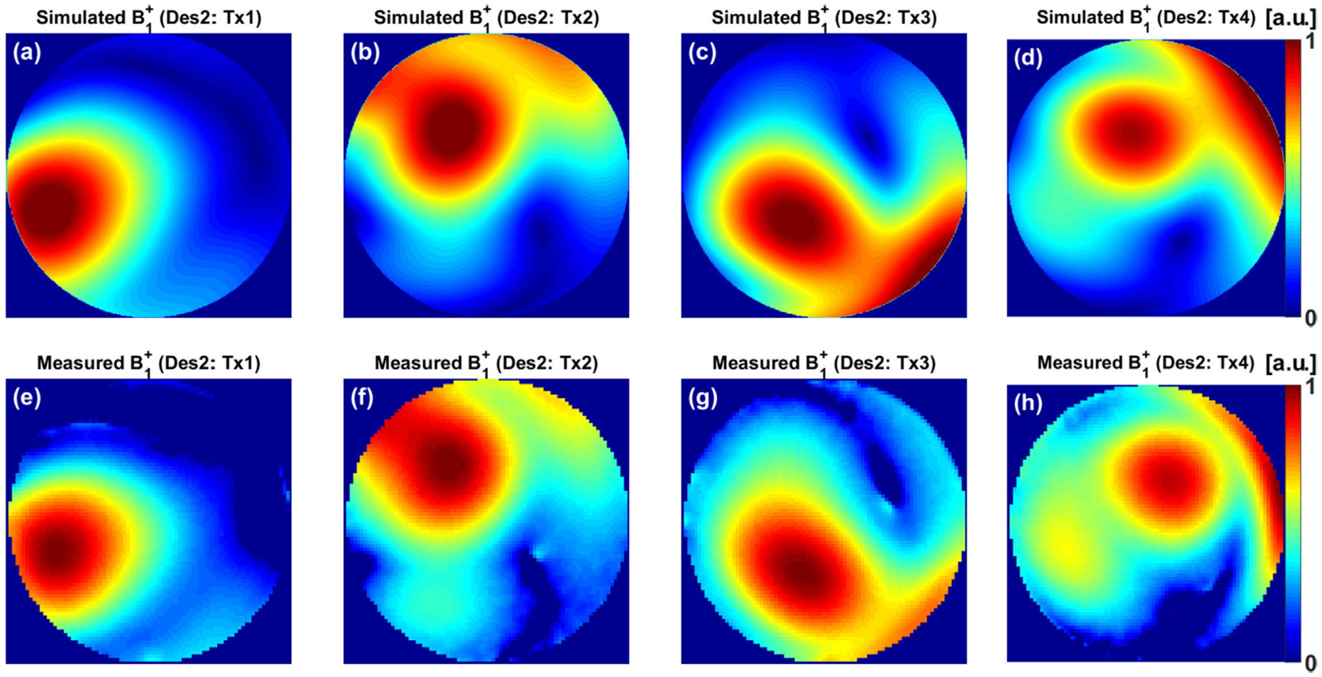

Fig. 3. Simulated and measured normalized central coronal B_1^+ field distributions for the individual four channels: T_{x1},T_{x2},T_{x3}, andT_{x4} of the anterior array of Design 2 within a 16 cm diameter spherical phantom. Simulation (a)–(d). Measurement (e)–(h).

for both coil array designs. Even with less elements from the L/R direction (three elements for Design 2 compared to four elements for Design 1), the antisymmetric array supports parallel imaging with acceleration factors up to R = 4 and keep the mean g-factor within the heart region of 1.13.

3.3.3. SNR and FA maps

The SNR evaluations from an *ex-vivo* pig experiment for both designs were obtained as part of the standard Siemens coil test procedures. The results representing SNR-map in a mid-ventricular short axis view of the pig thorax were shown in Fig. 7. The mean of the SNR was evaluated in the ROI of the heart for both combinations. The measured mean SNR values were 53.7 from the novel antisymmetric coil array compared to 21.2 from the rectilinear array. The novel antisymmetric array of Design 2 improved the SNR within the heart by about two times compared to standard Design 1. The spatial separation of the elements in the novel array with good decoupling and flexibility to bend the PCBs around the semi-half elliptical shaped housing resulted in a significant improvement in the SNR within the heart region. Additionally, the novel coil array demonstrates essentially better B_1^+ field homogeneity in the measured FA maps within heart regions

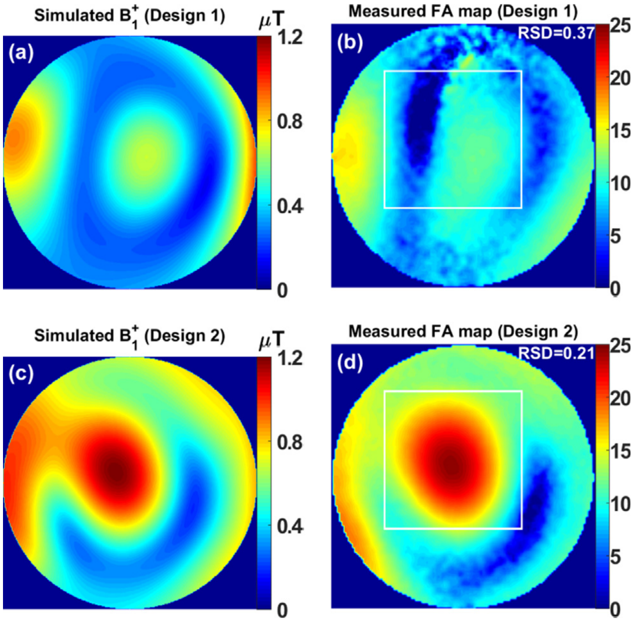

Fig. 4. Simulated and measured central coronal combined B_1^+ field distributions and the FA maps within a 16 cm diameter spherical phantom for Design 1 (a) & (b), Design 2 (c) & (d). Both anterior arrays were combined with the same rectilinear posterior array of Fig. 1e. The RSD of the FA maps were evaluated within the selected ROI. For both coil arrays, the total input power was 8 W.

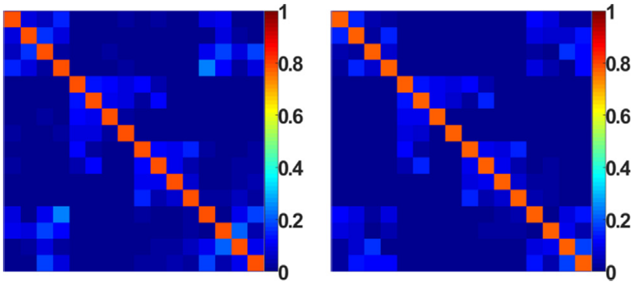

Fig. 5. Measured noise correlation matrices for an *ex-vivo* pig experiment acquired using Design 1 (left) and Design 2 (right). The maximum noise correlations are 0.24 and 0.18 for Design 1 and Design 2, respectively.

compared to the standard array design. The computed RSD was decreased from 0.65 from Design 1 to 0.46 for Design 2, which means about 30% improvement in FA homogeneity.

Fig. 8 shows high resolution *ex-vivo* short axis (SA) and long axis (LA) views of the pig heart acquired using Design 1 (left), and Design 2 (right), respectively. The novel cardiac array displayed a deeper penetration B_1^+ profile with less destructive interference (white arrows) over the entire heart of the pig compared to Design 1. Differences in signal intensities at the posterior wall of the left ventricle (LV) between the two designs are up to 45%. The novel array could provide better image quality in future *in-vivo* measurements.

3.4. Outlook of B_1^+ shimming for the cardiac arrays

To achieve the best possible image quality with the developed dedicated RF coil arrays for future *in-vivo* pig MR studies, comprehensive B_1^+ field optimizations of the RF shimming using the pig body phantom will be required.

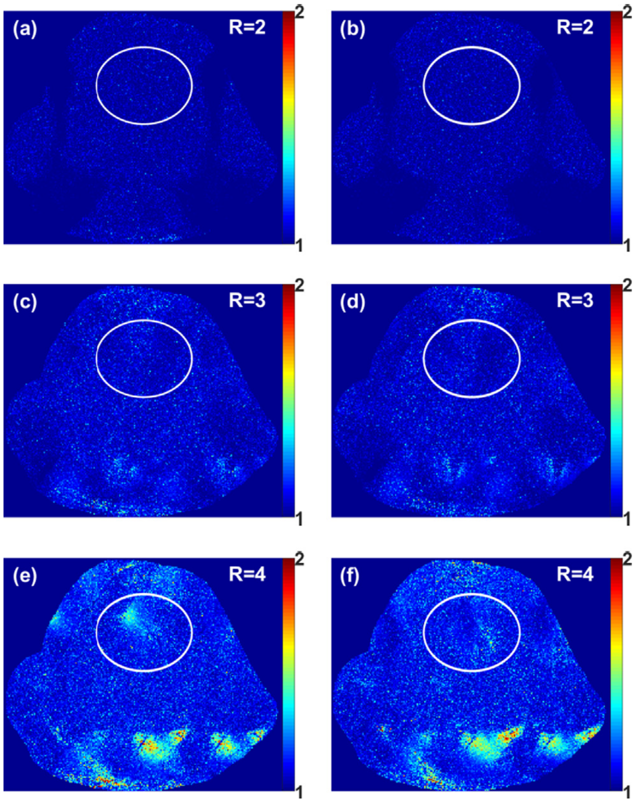

Fig. 6. Measured g-factor maps of R = 2, 3, and 4 for an *ex-vivo* pig experiment acquired using Design 1 (first column; (a), (c) and (e)), and for Design 2 (second column (b), (d) and (f)) with an acceleration in the L/R direction. The mean ± SD g-factor values were computed in the selected ROI as 1.03 ± 0.03, 1.06 ± 0.05, and 1.14 ± 0.09 for Design 1 and 1.03 ± 0.03, 1.06 ± 0.05, and 1.13 ± 0.07, respectively.

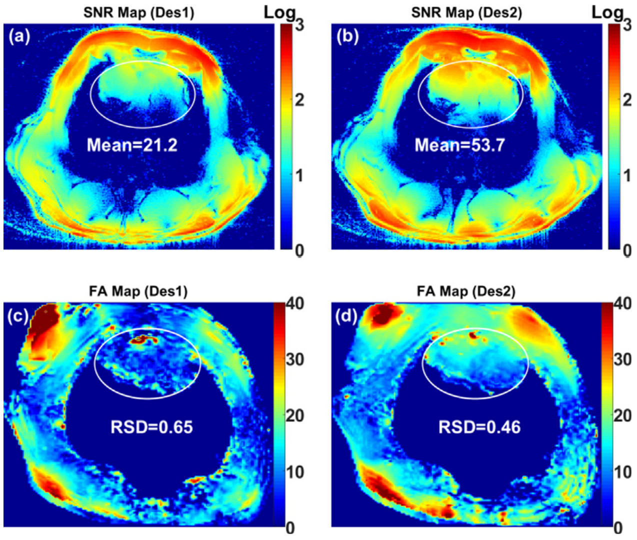

Fig. 7. Measured combined SNR maps in logarithmic scale (first row) and the combined FA maps in degrees (second row) acquired from Design 1 (a) & (c), and Design 2 (b) & (d).

3.4.1. Decorrelation analysis of the Tx-channels B_1^+ maps

Figs. 9 and 10 demonstrate the decorrelation analysis of four anterior Tx channels maps: T_{x1}, T_{x2}, T_{x3}, and T_{x4} for the standard rectilinear array and the novel antisymmetric array, respectively. The two row panels demonstrate: (first row) the normalized original B_1^+ maps, (second row) the B_1^+ maps after decorrelation. One can see that the decorrelation procedure essentially modifies two of four channels maps for Design 1 with new spatial harmonics appearing for T_{x3} and T_{x4}. In the same time, both 2D maps before and after decorrelation of the similar maps for the antisymmetric array show no modification of the spatial distribution of peak positions and profiles. Computed across summit points of B_1^+ maps, their shapes were preserved. For Design 1 decorrelation introduces minimal changes in T_{x1} and T_{x2}, whereas a significant modification of B_1^+ spatial distribution was observed for de-correlated maps in T_{x3} and T_{x4}. This confirms essential correlation of B_1^+ produced by these physical channels and, thus, reduction of degrees of freedom available for B_1^+ shimming. In contrast, for Design 2 there is practically no difference in original and de-correlated maps for all four channels. This confirms essentially higher independence of spatial harmonics of B_1^+ field produced by Design 2.

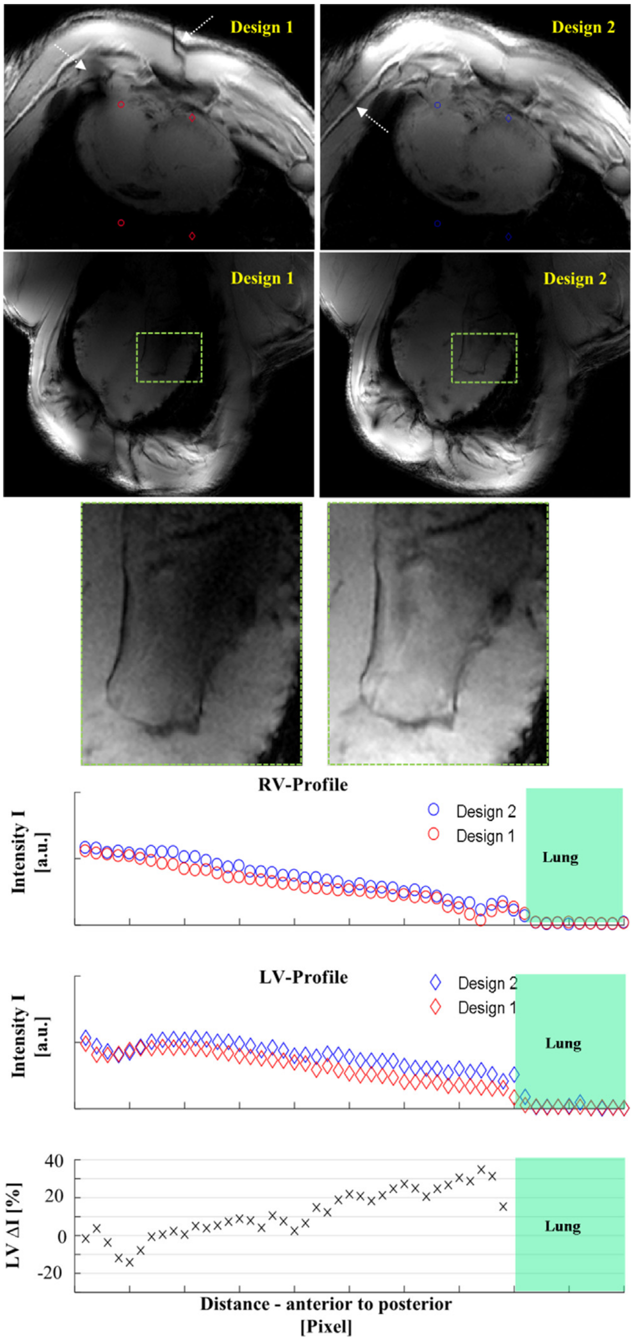

Fig. 8. High resolution (0.3 mm × 0.3 mm) *ex-vivo* SA and LA views of the pig heart acquired using Design 1 and Design 2. Plots in the upper right corner show profiles, connecting the anterior and posterior red and blue points respectively. The difference between the two designs is plotted in percentage for the profile through the left ventricle. Areas of destructive interference in the short axis images are indicated by white arrows. (For interpretation of the references to colour in this figure legend, the reader is referred to the web version of this article.)

3.4.2. Static B_1^+ shimming

The results of the global search of the hard-wired phase set performed for Design 1 and 2 were shown in Fig. 11. The simulated transversal combined B_1^+ field distributions within the pig body phantom for Design 1 and Design 2 before RF shimming and after RF shimming were shown in Fig. 12. The transversal, B_1^+ fields were computed for the optimal phase vectors Φ providing optimal targeted B_1^+ field found by solving the optimization problem (3). The angular diagrams showing corresponding phase vector components. The important statistical characteristic of the B_1^+ field contributing cost function are inverse relative standard deviation, mean value of B_1^+ and transmission efficiency Tx_{eff}. Maximizing of this value ensures homogeneity of the B_1^+ distribution in the optimization region Δr, and achieving necessary FA with minimal necessary power. These values were found to be (3.2, 0.34, and 0.44) versus (2.95, 0.42, and 0.52) for Design 1 and 2, respectively. The product of these three values could be considered as "coil performance index" which is 20% better for Design 2 in comparison to Design 1.

4. Discussion

In this work, we have presented a novel antisymmetric Tx/Rx coil array to demonstrate the feasibility of cMRI in pigs at 7 T. The antisymmetric array was compared to a standard rectilinear coil array optimized for a 50 kg pig, where the housing fits well to the thorax shape. Both coils have been designed to have a curved housing for both anterior and posterior sections. EM simulations were performed and validated for all individual channels of both anterior arrays and for the combined B_1^+ field for all eight channels, while keeping the same posterior array without moving to show the advantages of the antisymmetric array versus the standard rectilinear array. High resolution *ex-vivo* cardiac images were acquired with an in-plane resolution of up to 0.3 mm × 0.3 mm using both arrays. Parallel imaging with R = 4 in the L/R direction is possible using the novel antisymmetric array, while maintaining a mean g-factor of 1.13 within the heart region.

4.1. Symmetric versus antisymmetric coil array design

Performing cMRI at 7 T requires a multichannel Tx/Rx coil array combining an arrangement of multiple individual elements in different shapes, different element sizes, and different physical orientations in order to homogenize the B_1^+ field within the heart region. To enable RF shimming and to improve the transmit B_1^+ field uniformity for cMRI at 7 T, each coil element should have its individual and unique transmit B_1^+ field and receive sensitivity. The multichannel Tx/Rx arrays based on rectilinear loop configurations could have coupling between the diagonal elements (Table 2). Therefore, we proposed in this work, a novel antisymmetric array coil design based on mirrored and reversed loop elements aiming to minimize coupling between all neighboring loops through the entire coil array (Table 3). In this paper, the dimensions of the coil elements were chosen as described in [47]. Instead of extending the elements in the longitudinal direction like in Design 1, six elements of Design 2 (the elements 3, 4, 5, 6, 7 and 8) were extended in the transversal direction (Fig. 1c). The penetration of the B_1^+ field was stronger (Fig. 8) from those elements after bending of the elements.

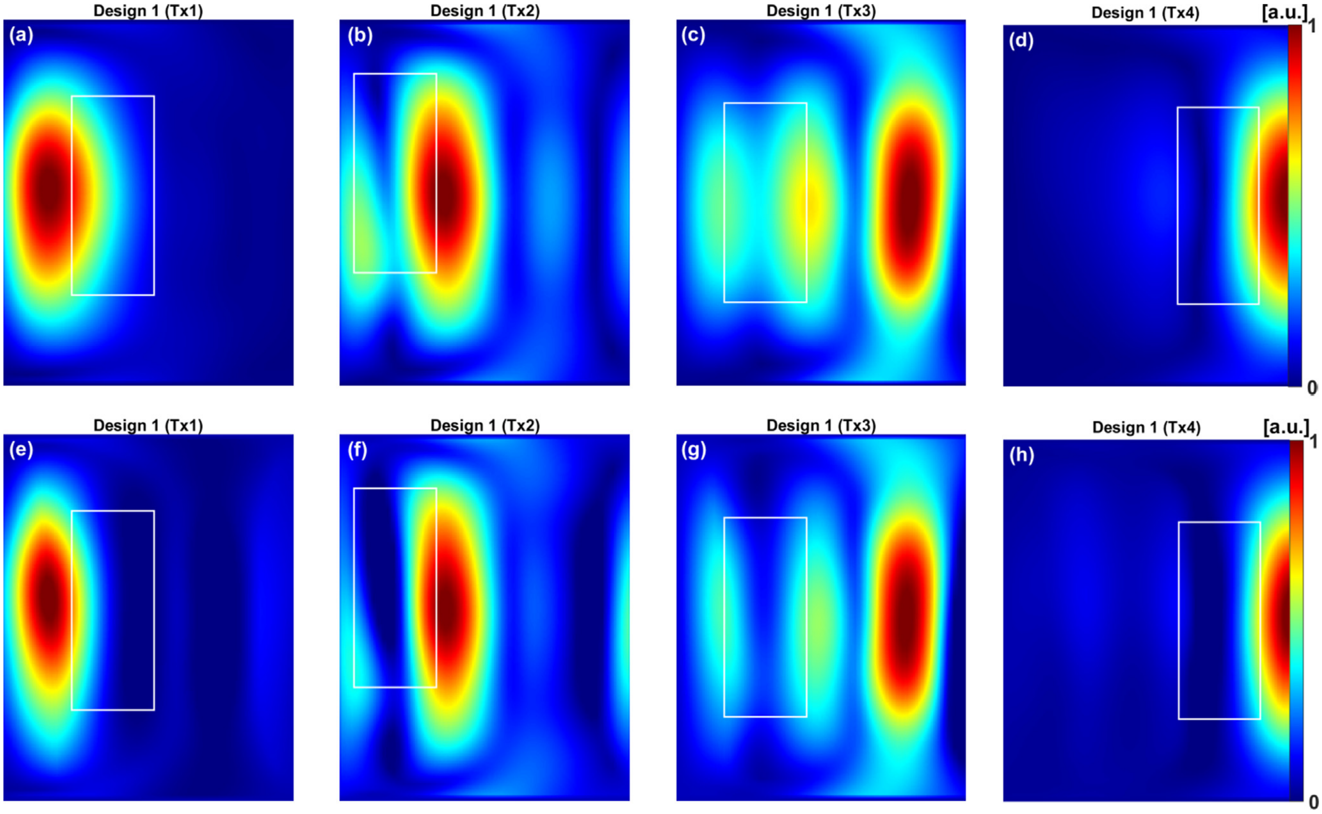

Fig. 9. Simulated multiband decorrelation performed on the original normalized coronal B_1^+ field at 10 cm from coil surface within the pig body phantom for the individual four channels of the anterior array of Design 1 (T_{x1},T_{x2},T_{x3}, andT_{x4}) (a)–(d) and the de-correlated normalized B_1^+ field (e)–(h).

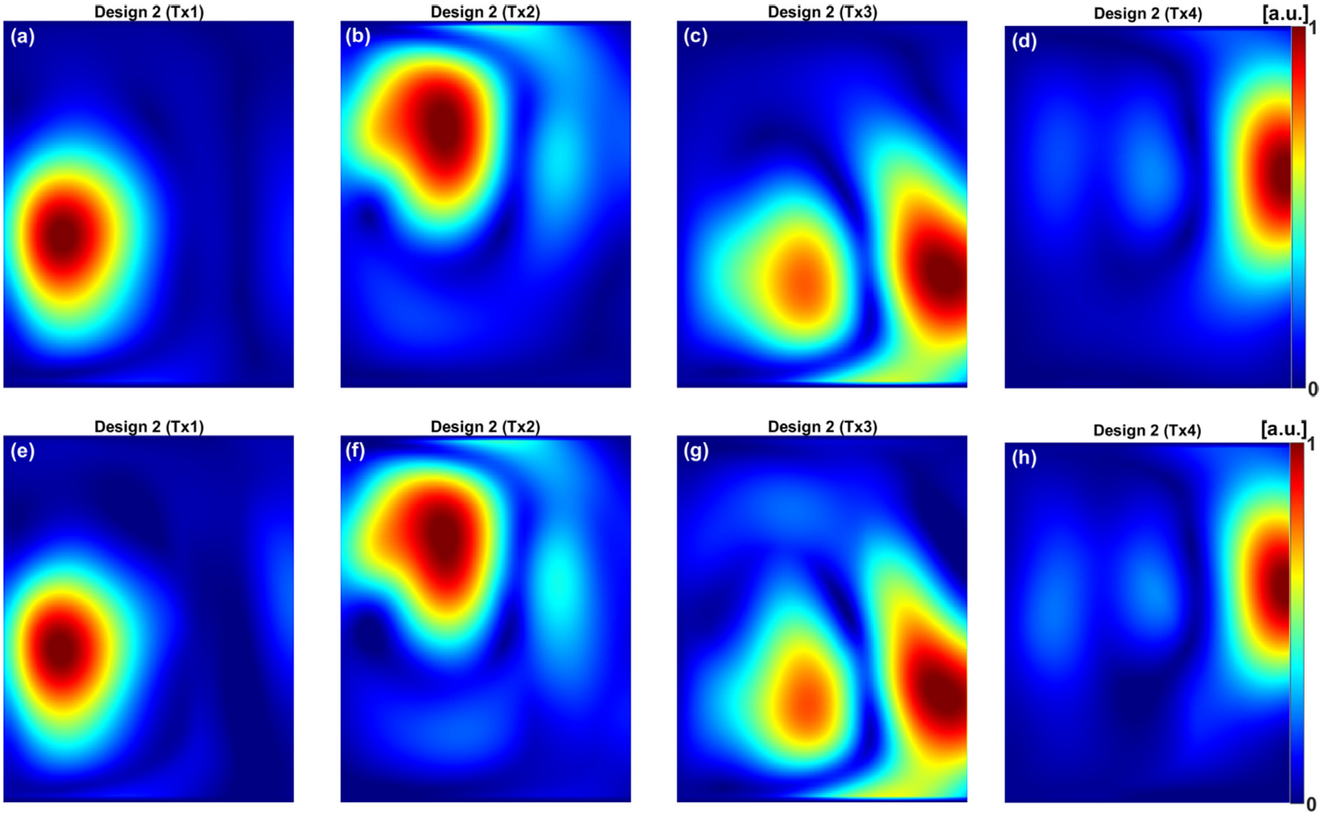

Fig. 10. Simulated multiband decorrelation performed on the original normalized coronal B_1^+ field at 10 cm from coil surface within the pig body phantom for the individual four channels of the anterior array of Design 2 (T_{x1},T_{x2},T_{x3}, andT_{x4}) (a)–(d) and the de-correlated normalized B_1^+ field (e)–(h).

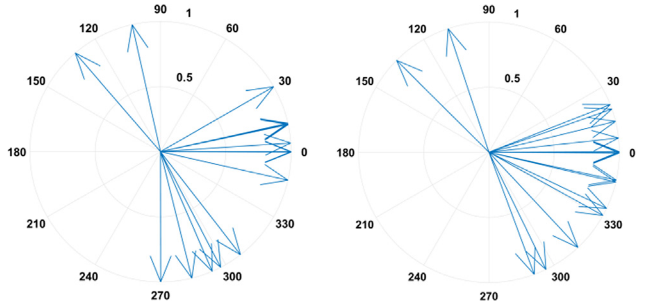

Fig. 11. Optimal phase vector components for Design 1 (left) and Design 2 (right) were optimized within the pig body phantom.

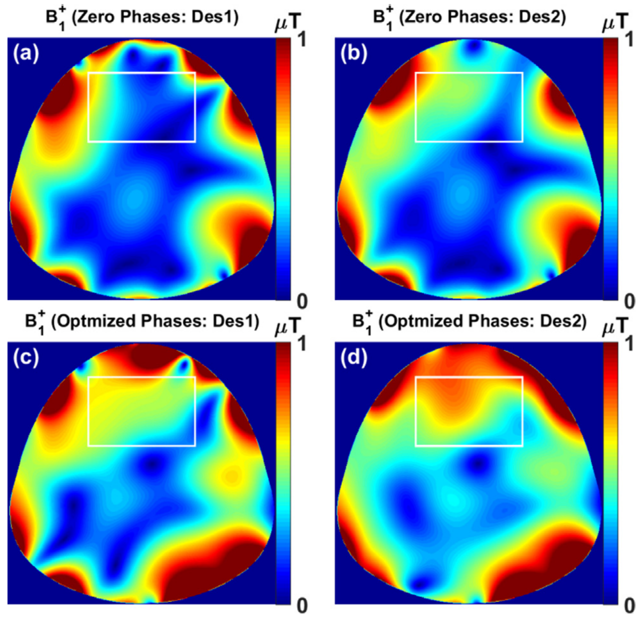

Fig. 12. Simulated combined B_1^+ field distributions within the pig body phantom for Design 1 (first column) and Design 2 (second column) with zero phases (a) & (b) and after shimming (c) & (d).

4.2. MR measurements

The antisymmetric array Design 2 provides a varying coronal B_1^+ field profiles at different geometrical locations within the phantom compared to Design 1 (Figs. 2 and 3). For Design 1, the B_1^+ field distribution per channel shows some magnetic coupling for both channels T_{x3} and T_{x4} in a 16 cm diameter spherical phantom (Fig. 2c, d, g, and h). The observed discrepancy between simulations and MR measurements are most probably not related to electrical coupling because there is no evidence of electric coupling in the measured S-matrix in both phantom and in *ex-vivo* pig. This is most probably effect of distribution of the B_1^+ field in the specific spherical phantom. We performed additionally the multiband decorrelation analysis of B_1^+ field for the pTx-channels combinations of both designs in order to reveal the correlations presented in the individual channels B_1^+ field profiles. The simulation was done using elliptical phantom which provide best possible loading of all elements was used in the numeric simulation. The discrepancy between simulation and MR measurements has many reasons. First, it may be due to a variation of the phantom geometry and position with respect to the coil. Second, in CST simulations, the PSs and cable traps were not taken into account because they were considered to be ideal 50 Ω circuits. However, in the real coil it is possible that the input impedance of the element changes. Third, the intrinsic error in the DAM FA-mapping is at least 5% because it is based on the division of two images which, increases error propagation. Finally, the relative phases for each element were measured at 9.5 cm distance from the element surface; however, the phases may change at the center of the spherical dielectric phantom.

The developed coil array demonstrates essentially better B_1^+ field homogeneity in the measured FA maps within heart region by about 30% (Fig. 7d), good decoupling between neighboring element and distinct B_1^+ field localizations in phantom measurements (Figs. 3 and 4) compared to the standard rectilinear loop design, which could be efficient for RF shimming for cMRI in future *in-vivo* pig experiments at 7 T. Parallel imaging with acceleration factors up to R = 4 were feasible with reasonable mean g-factor of 1.13 measured in the heart region. The novel antisymmetric coil array provides lower noise amplification values (1.13 ± 0.07) with GRAPPA acceleration factors of R = 4 compared to the typically measured g-factors (1.58 ± 0.43, 2.33 ± 0.50, and 1.2) using 8-channel [28], 16-channel [29] and 32-channel [24] Tx/Rx loop human coil arrays, respectively. The novel coil array design offers improved B_1^+ penetration within the heart region of the pig compared to the standard rectilinear array design. The thorax-matched shape of the housing, the optimized element dimensions, and the novel decoupling scheme improved B_1^+ and B_1^- field profiles in comparison with the ones achieved using the traditional rectilinear arrays at 7 T.

The novel antisymmetric array enhanced the SNR in an *ex-vivo* measurement of the heart by about two-fold compared to standard rectilinear array design (Fig. 7). To the best of our knowledge, the in-plane high resolution of 0.3 mm × 0.3 mm cardiac images that we acquired using the dedicated pig array are among the top obtained so far for cMRI at 7 T in humans or in large animals (Fig. 8). Improved sensitivity of the dedicated pig coil array enabled the acquisition of cardiac images with a resolution up to three times higher than typically acquired resolutions at 3 T using human receive surface coils [51–53]. Simulation results regarding RF-shimming (Fig. 12) show that the antisymmetric coil array will perform well in *in-vivo* measurements using the pTx system.

Recent developments demonstrated the benefits of using dipole antenna arrays for body imaging at 7 T [31–35]. Dipole antennas have higher penetration depth inside the body compared to the traditional loop elements and are thus suited for organs such as the heart. Combining dipole antennas and loops has the potential to increase both receive sensitivity and transmit performance for body imaging [38] and cMRI at 7 T [39]. Further improvement of the proposed antisymmetric coil design is possible by increasing the number of elements of the array on the same PCB to 16 or even higher with 32 elements, while keeping good decoupling between all elements and distinct B_1^+ field localizations. A 16-channnel antisymmetric loop array for the anterior section could be combined with a 16-channel dipole antenna array for the posterior section to form 32 channel coil array. This combination could help to improve both transmit and receive efficiency for cMRI at 7 T.

4.3. Contribution of the B_1^+ field from the posterior array to the total transmit B_1^+ field

A posterior array from the novel antisymmetric design has been designed, implemented, and tested only in a spherical phantom. Phantom MRI measurements have been performed using the anterior part of Design 2 in combination with both the rectilinear array Design 1 and the novel antisymmetric array Design 2 type as posterior array part (the results can be found in supplementary materials Fig. 1). The combined B_1^+ field was measured in the center of the phantom sphere (at 10 cm from anterior array and about 15 cm from posterior array). One can see that there is only minimal difference on B_1^+ field when the posterior array was changed from Design 1 to Design 2 antisymmetric type. This confirms that the effect of posterior array design on the B_1^+ field distribution at the targeted region is minimal and therefore the only Design 1 was used in the *ex-vivo* test. These, in particular, ensured the fixed position of the pig body in the MRI comparison tests. While anterior array parts could be changed without pig body repositioning, the changing of posterior array would lead to re-allocation of the pig body and thus missing the MRI slice position localization relative to the scanner reference system. The contribution of the transmit B_1^+ field from the posterior array to the total B_1^+ field was about 10% with the animal in place. As a result, building a second posterior array from the same novel design was considered of minor importance.

4.4. Decorrelation analysis of the Tx-channels B_1^+ maps

The PCA-based decorrelation analysis has additionally proven the advantages of the Design 2 in comparison with Design 1 in terms of usage for static and dynamic pTx-shimming. The changes in shape of the de-correlated B_1^+ spatial harmonics formed by two Tx-channels T_{x3} andT_{x4} proved that the initial B_1^+ distribution in physical channels were significantly correlated and, thus, limiting the degrees of freedom available for B_1^+ shimming. This is especially remarkable in the gap zones between elements. In the same time the de-correlated B_1^+ maps for Design 2 shows very little difference with the original physical channel maps, where the 2D profiles were identical before and after decorrelation. This confirms that both configuration of elements in Design 2 and its distribution within available Tx channels were optimal and provide optimal flexibility for B_1^+ shimming via maximization of the dynamic range and minimization of the correlation of spatial harmonics formed by individual Tx channels.

4.5. Static B_1^+shimming

The phase vector optimization results reveal the significant advantage of Design 2 in terms of static B_1^+ shimming optimization potential (Fig. 12). The larger amount of degrees of freedom available for optimization provides more than factor 1.5 larger mean B_1^+ values in the transversal projections of the optimized region whereas the difference of mean and maximal value characterizing targeted B_1^+ homogeneity was practically the same in both cases. The second important factor of Design 2 was the smaller spread of the optimal phase vector components in comparison to Design 1 (Fig. 11). This leads to an improvement of the transmit efficiency factor and, thus, additionally increased of maximal and mean B_1^+ values.

5. Conclusions

In this paper, the design, simulation, assembly and testing of a novel antisymmetric array for cMRI in pigs at 7 T have been described. The antisymmetric array has demonstrated good decoupling provided by the reversed and mirrored geometrical loop orientations and improved control of the B_1^+ field distributions for efficient RF shimming. The antisymmetric coil array improved the SNR by about two times within the heart region compared to the regular symmetric coil array. The main achievement of the novel dedicated pig coil array was the possibility to obtain cardiac images with high in-plane resolution (0.3 mm × 0.3 mm), with high SNR, B_1^+ field homogeneity within the heart, and the possibility of sophisticated B_1^+ shimming. Using the novel antisymmetric coil design it is possible to increase the number of elements of the array on the same PCB to 16 or even 32 elements, while keeping good decoupling between all elements and distinct B_1^+ field localizations.

Acknowledgement

This project is funded by the German Ministry of Education and Research (BMBF) with grant # 01EO1004 & 01EO1504. We would like to thank Dr. S. Baltes for providing us with the *ex-vivo* pig.

Appendix A

See Tables 2–7.

Table 2
Simulated (yellow) and measured S-Matrix in dB for the dedicated pig coil array (Design 1) loaded with a 16 cm spherical dielectric phantom combined with six rectangular bottles with $\varepsilon_r = 59.3$, $\sigma = 0.79$ S/m.

Ch.	1	2	3	4	5	6	7	8	9	10	11	12	13	14	15	16	Ch.
	−18	−18	−15	−10	−21	−14	−20	−16	−33	−22	−31	−32	−32	−34	−34	−36	1
		−25	−10	−16	−14	−20	−17	−21	−35	−23	−35	−31	−42	−30	−29	−27	2
1	−13		−23	−15	−12	−15	−16	−18	−50	−30	−33	−35	−34	−34	−32	−41	3
2	−9.0	−18		−15	−15	−11	−17	−14	−39	−40	−40	−38	−42	−37	−38	−32	4
3	−20	−11	−7.0		−27	−23	−13	−9.0	−32	−37	−34	−35	−34	−34	−34	−35	5
4	−11	−21	−28	−11		−25	−10	−17	−40	−35	−38	−37	−45	−34	−52	−36	6
5	−19	−20	−19	−14	−10		−17	−18	−37	−30	−36	−52	−38	−32	−32	−27	7
6	−19	−19	−15	−18	−27	−9.0		−29	−30	−27	−41	−31	−37	−28	−35	−32	8
7	−20	−23	−20	−18	−19	−11	−13		−13	−16	−19	−18	−24	−27	−24	−27	9
8	−24	−20	−22	−18	−11	−21	−9.0	−20		−8.0	−19	−21	−30	−21	−28	−26	10
9	−24	−30	−32	−35	−36	−37	−32	−38	−14		−6.0	−16	−16	−25	−26	−28	11
10	−29	−24	−36	−32	−35	−39	−38	−31	−26	−7.0		−6.0	−27	−16	−27	−23	12
11	−24	−29	−31	−38	−33	−35	−30	−38	−19	−20	−10		−6.0	−18	−24	−19	13
12	−28	−24	−36	−32	−34	−36	−35	−28	−20	−21	−14	−7.0		−6.0	−18	−24	14
13	−30	−39	−34	−35	−31	−38	−25	−29	−25	−33	−17	−24	−7.0		−11	−20	15
14	−36	−28	−35	−35	−36	−32	−28	−24	−34	−26	−24	−17	−15	−7.0		−10	16
15	−32	−40	−37	−36	−31	−36	−25	−29	−30	−36	−25	−34	−20	−20	−10		
16	−39	−31	−36	−39	−35	−33	−30	−24	−35	−32	−34	−26	−21	−21	−26	−6.0	
	1	2	3	4	5	6	7	8	9	10	11	12	13	14	15	16	

Table 3
Simulated (yellow) and measured S-Matrix in dB for the dedicated pig coil array (Design 2) loaded with a 16 cm spherical dielectric phantom combined with six rectangular bottles with $\varepsilon_r = 59.3$, $\sigma = 0.79$ S/m.

Ch.	1	2	3	4	5	6	7	8	9	10	11	12	13	14	15	16	Ch.
	−16	−24	−23	−13	−16	−16	−17	−18	−33	−36	−32	−35	−34	−34	−33	−39	1
		−20	−15	−21	−18	−17	−18	−19	−38	−37	−36	−34	−32	−34	−36	−33	2
1	−9.0		−9.0	−25	−14	−17	−18	−14	−27	−24	−30	−29	−34	−27	−34	−28	3
2	−20	−9.0		−12	−20	−12	−15	−13	−34	−41	−29	−36	−28	−32	−28	−27	4
3	−26	−18	−10		−12	−18	−12	−18	−34	−30	−34	−33	−32	−35	−29	−29	5
4	−18	−26	−31	−10		−10	−27	−11	−33	−42	−36	−44	−34	−41	−34	−34	6
5	−24	−19	−16	−19	−20		−8.0	−39	−32	−30	−28	−35	−28	−36	−27	−35	7
6	−19	−25	−19	−16	−21	−20		−8.0	−31	−34	−39	−33	−34	−31	−29	−33	8
7	−19	−21	−18	−13	−14	−22	−7.0		−14	−16	−20	−18	−24	−29	−26	−27	9
8	−21	−19	−13	−17	−22	−14	−28	−9.0		−9.0	−20	−23	−30	−23	−29	−27	10
9	−37	−47	−33	−28	−31	−42	−24	−35	−13		−6.0	−17	−16	−28	−25	−40	11
10	−49	−37	−26	−38	−32	−44	−33	−31	−29	−7.0		−6.0	−26	−16	−29	−23	12
11	−37	−46	−33	−26	−32	−40	−24	−40	−19	−21	−10		−6.0	−17	−23	−20	13
12	−47	−37	−25	−48	−32	−45	−35	−27	−20	−21	−15	−7.0		−6.0	−18	−26	14
13	−37	−47	−45	−24	−42	−31	−28	−34	−25	−34	−17	−25	−7.0		−13	−18	15
14	−45	−38	−27	−35	−40	−34	−43	−24	−34	−27	−25	−17	−15	−6.0		−9.0	16
15	−37	−47	−38	−25	−42	−32	−31	−32	−31	−36	−25	−35	−20	−21	−10		
16	−47	−37	−30	−34	−43	−33	−37	−25	−35	−33	−34	−27	−22	−21	−29	−6.0	
	1	2	3	4	5	6	7	8	9	10	11	12	13	14	15	16	

Table 4
Simulated S-Matrix in dB for the dedicated pig coil array (Design 1) loaded with the pig body phantom with $\varepsilon_r = 59.3$, $\sigma = 0.79$ S/m.

Ch.	1	2	3	4	5	6	7	8	9	10	11	12	13	14	15	16
1	−15															
2	−19	−12														
3	−20	−17	−12													
4	−15	−21	−20	−10												
5	−26	−32	−17	−17	−10											
6	−30	−28	−17	−16	−20	−10										
7	−40	−31	−26	−30	−21	−15	−15									
8	−31	−42	−32	−28	−17	−21	−19	−12								
9	−50	−46	−45	−47	−48	−55	−47	−68	−15							
10	−46	−49	−46	−44	−55	−47	−63	−47	−29	−19						
11	−41	−46	−48	−60	−49	−52	−47	−54	−20	−20	−16					
12	−45	−42	−66	−48	−52	−50	−52	−47	−20	−20	−18	−12				
13	−46	−53	−49	−52	−48	−59	−41	−46	−34	−37	−16	−25	−12			
14	−52	−47	−52	−50	−64	−48	−45	−42	−36	−35	−25	−16	−18	−12		
15	−47	−69	−47	−55	−45	−47	−50	−46	−40	−40	−35	−36	−21	−20	−16	
16	−65	−47	−54	−47	−46	−44	−46	−49	−40	−40	−35	−35	−20	−20	−29	−19

Table 5
Simulated S-Matrix in dB for the dedicated pig coil array (Design 2) loaded with the pig body phantom with $\varepsilon_r = 59.3$, $\sigma = 0.79$ S/m.

Ch.	1	2	3	4	5	6	7	8	9	10	11	12	13	14	15	16
1	−10															
2	−18	−10														
3	−44	−17	−13													
4	−17	−43	−35	−13												
5	−22	−21	−18	−27	−23											
6	−21	−22	−27	−18	−25	−23										
7	−18	−32	−27	−23	−14	−37	−14									
8	−32	−18	−23	−27	−37	−14	−33	−14								
9	−46	−54	−58	−44	−48	−47	−43	−50	−18							
10	−54	−46	−44	−59	−47	−48	−50	−43	−32	−18						
11	−63	−47	−45	−52	−52	−51	−59	−47	−32	−30	−12					
12	−47	−63	−52	−45	−51	−52	−47	−59	−30	−31	−40	−14				
13	−51	−46	−48	−47	−50	−50	−48	−48	−18	−21	−21	−32	−12			
14	−46	−51	−47	−48	−50	−50	−48	−48	−21	−18	−32	−21	−24	−12		
15	−47	−53	−61	−48	−52	−48	−48	−51	−16	−25	−28	−28	−16	−31	−11	
16	−53	−47	−48	−61	−48	−52	−51	−48	−25	−16	−28	−28	−31	−16	−47	−11

Table 6
Optimized capacitor values in pF obtained using CST RF-circuit co-simulation loaded with the pig body phantom and optimized on bench-top measurements for the anterior array of Design 1 loaded with a 46 kg *ex-vivo* pig. All capacitor variables and values are corresponding to Fig. 1a.

Capacitor	Bench	Simulation	Deviation
C_1^d	12.7	12.7	0%
C_2^d	14.7	14.7	0%
C_3^d	1.60	1.60	0%
C_1^t	5.20	5.20	0%
C_2^t	4.70	4.70	0%
C_1^m	10.0	10.0	0%
C_2^m	6.20	6.20	0%
C_3^m	6.20	6.20	0%
C_4^m	6.20	6.20	0%
C_5^m	6.20	6.20	0%
C_6^m	6.20	6.20	0%
C_7^m	10.0	10.0	0%
C_8^m	6.20	6.20	0%
C_1^a	10.0	10.0	0%
C_2^a	10.0	10.0	0%
C_3^a	8.20	8.20	0%
C_4^a	8.20	8.20	0%
C_5^a	8.20	8.20	0%
C_6^a	8.20	8.20	0%
C_7^a	10.0	10.0	0%
C_8^a	10.0	10.0	0%
C_1^b	18.2	18.2	0%
C_2^b	16.4	16.4	0%
C_3^b	10.0	10.0	0%
C_4^b	11.0	11.0	0%
C_5^b	11.0	11.0	0%
C_6^b	10.0	10.0	0%
C_7^b	18.2	18.2	0%
C_8^b	16.4	16.4	0%

Table 7
Optimized capacitor values in pF obtained using CST RF-circuit co-simulation loaded with the pig body phantom and optimized on bench-top measurements for the novel antisymmetric array Design 2 loaded with a 46 kg *ex-vivo* pig. All capacitor variables and values are corresponding to Fig. 1c.

Capacitor	Bench	Simulation	Deviation
C_1^d	18.2	18.2	0%
C_2^d	12.7	12.7	0%
C_3^d	8.00	8.00	0%
C_4^d	4.70	4.70	0%
C_5^d	1.60	1.60	0%
C_6^d	1.00	1.00	0%
C_7^d	2.10	2.10	0%
C_1^t	10.5	10.5	0%
C_2^t	6.20	6.20	0%
C_3^t	3.30	3.30	0%
C_4^t	10.0	10.0	0%
C_5^t	8.20	8.20	0%
C_6^t	6.20	6.20	0%
C_1^m	4.70	6.20	32%
C_2^m	4.70	6.20	32%
C_3^m	8.20	8.20	0%
C_4^m	8.20	8.20	0%
C_5^m	10.0	8.20	22%
C_6^m	10.0	8.20	22%
C_7^m	8.20	8.20	0%
C_8^m	8.20	8.20	0%
C_1^a	10.0	10.0	0%
C_2^a	10.0	10.0	0%
C_3^a	8.20	8.20	0%
C_4^a	8.20	8.20	0%
C_5^a	6.20	6.20	0%
C_6^a	6.20	6.20	0%
C_7^a	8.20	8.20	0%
C_8^a	8.20	8.20	0%
C_1^b	18.2	16.2	14%
C_2^b	19.2	16.2	18%
C_3^b	10.5	10.5	0%
C_4^b	11.0	10.5	0%
C_5^b	8.20	8.20	0%
C_6^b	7.80	8.20	12%
C_7^b	8.70	8.20	06%
C_8^b	9.50	8.20	12%

Appendix B. Supplementary material

Supplementary data to this article can be found online at https://doi.org/10.1016/j.jmr.2019.07.004.

References

[1] E. Yacoub et al., Imaging brain function in humans at 7 tesla, Magn. Reson. Med. 45 (4) (2001) 588–594.

[2] J.T. Vaughan et al., 7 T versus 4 T: RF power, homogeneity, and signal-to-noise comparison in head images, Magn. Reson. Med. 24 (1) (2001) 24–30.

[3] T.S. Ibrahim, R. Lee, A.M. Abduljalil, B.A. Baertlein, P.-M.L. Robitaille, Dielectric resonances and B_1 field inhomogeneity in UHFMRI: computational analysis and experimental findings, Mag. Reson. Imag. 19 (2) (2001) 219–226.

[4] Q.X. Yang et al., Analysis of wave behavior in lossy dielectric samples at high field, Magn. Reson. Med. 47 (5) (2002) 982–989.

[5] P.F. Van de Moortele et al., B_1 destructive interferences and spatial phase patterns at 7 T with a head transceiver array coil, Magn. Reson. Med. 54 (6) (2005) 1503–1518.

[6] T.S. Ibrahim et al., Design and performance issues of RF coils utilized in ultra high field MRI: experimental and numerical evaluations, IEEE Trans. Biomed. Eng. 52 (7) (2005) 1278–1284.

[7] X. Zhang et al., Microstrip RF surface coil design for extremely high field MRI and spectroscopy, Magn. Reson. Med. 46 (3) (2001) 443–450.

[8] J.T. Vaughan et al., High-frequency volume coils for clinical NMR imaging and spectroscopy, Magn. Reson. Med. 32 (2) (1994) 206–218.

[9] X. Zhang et al., An inverted-microstrip resonator for human head proton MR imaging at 7 tesla, IEEE Trans. Biomed. Eng. 52 (3) (2005) 495–504.

[10] X.L. Zhang et al., A microstrip transmission line volume coil for human head MR imaging at 4 T, J. Magn. Reson. 161 (2) (2003) 242–251.

[11] X. Zhang et al., Higher-order harmonic transmission-line RF coil design for MR applications, Magn. Reson. Med. 53 (5) (2005) 1234–1239.

[12] B. Wu et al., Multi-channel microstrip transceiver arrays using harmonics for high field MR imaging in humans, IEEE Trans. Med. Imag. 31 (2) (2012) 183–191.

[13] B. Wu et al., Shielded microstrip array for 7 T human MR imaging, IEEE Trans. Med. Imag. 29 (1) (2010) 179–184.

[14] C.E. Akgun et al., Novel multi-channel transmission line coil for high field magnetic resonance imaging, in: IEEE MTT-S Int. Microw. Symp. Dig., Boston, MA, USA, Jun. 2009, 2009, pp. 1425–1428.

[15] C.E. Akgun et al., Alternating impedance multi-channel transmission line resonators for high field magnetic resonance imaging, in: IEEE MTT-S Int. Microw. Symp. Dig., May 2010, pp. 756–759.

[16] S.-M. Sohn, L. DelaBarre, J.T. Vaughan, A. Gopinath, RF multichannel head coil design with improved B1+ Fields uniformity for high field MRI systems, in: IEEE MTT-S Int. Microw. Symp. Dig., Jun. 2012, 2012, pp. 1–3.

[17] I.A. Elabyad, A. Omar, An investigation of alternating impedance microstrip transceiver coil arrays for MRI at 7 T, in: IEEE MTT-S Int. Microw. Symp. Dig., Baltimore, MD, USA, Jun. 2011, 2011, pp. 1–4.

[18] S.-M. Sohn, L. DelaBarre, A. Gopinath, J.T. Vaughan, RF head coil design with improved RF magnetic near-fields uniformity for magnetic resonance imaging (MRI) systems, IEEE Trans. Microw. Theory Techn. 62 (8) (2014) 1784–1789.

[19] C.E. Akgun et al., Stepped impedance resonators for high-field magnetic resonance imaging, IEEE Trans. Biomed. Eng. 61 (2) (2014) 327–333.

[20] Z. Chen, K. Solbach, D. Erni, A. Rennings, Improving Efficiency and signal-to-noise-ratio of a surface coil by a high-impedance-surface RF shield for 7-T magnetic resonance imaging, IEEE Trans. Microw. Theory Technol. 65 (3) (2017) 988–997.

[21] Z. Chen, K. Solbach, D. Erni, A. Rennings, Electromagnetic field analysis of a dipole coil element with surface impedance characterized shielding plate for 7-T MRI, IEEE Trans. Microw. Theory Technol. 64 (3) (2016) 972–981.

[22] C.J. Snyder et al., Initial results of cardiac imaging at 7 Tesla, Magn. Reson. Med. 61 (3) (2009) 517–524.

[23] J.T. Vaughan et al., Whole-body imaging at 7T: preliminary results, Magn. Reson. Med. 61 (1) (2009) 244–248.

[24] A. Graessl et al., Modular 32-channel transceiver coil array for cardiac MRI at 7.0T, Magn. Reson. Med. 72 (1) (2014) 276–290.

[25] M.A. Dieringer et al., Design and application of a four-channel transmit/receive surface coil for functional cardiac imaging at 7T, J. Magn. Reson. Imag. 33 (3) (2011) 736–741.

[26] L. Winter et al., Comparison of three multichannel transmit/receive radiofrequency coil configurations for anatomic and functional cardiac MRI at 7.0T: implications for clinical imaging, Eur. Radiol. 22 (10) (2012) 2211–2220.

[27] T. Niendorf et al., Progress and promises of human cardiac magnetic resonance at ultrahigh fields: a physics perspective, J. Magn. Reson. 229 (2013) 202–222.

[28] A. Gräßl et al., Design, evaluation and application of an eight channel transmit/receive coil array for cardiac MRI at 7.0T, Eur. J. Radiol. 82 (5) (2013) 752–759.

[29] C. Thalhammer et al., Two-dimensional sixteen channel transmit/receive coil array for cardiac MRI at 7.0 T: design, evaluation, and application, J. Magn Reson Imag. 36 (4) (2012) 847–857.

[30] M.J. Versluis, N. Tsekos, N.B. Smith, A.G. Webb, Simple RF design for human functional and morphological cardiac imaging at 7 tesla, J. Magn Reson 200 (1) (2009) 161–166.

[31] A.J.E. Raaijmakers et al., Design of a radiative surface coil array element at 7 T: the single-side adapted dipole antenna, Magn. Reson. Med. 66 (5) (2011) 1488–1497.

[32] A.J. Raaijmakers et al., The fractionated dipole antenna: a new antenna for body imaging at 7 Tesla, Magn. Reson. Med. 75 (3) (2016) 1366–1374.

[33] Q. Duan et al., A 7T spine array based on electric dipole transmitters, Magn. Reson. Med. 74 (4) (2015) 1189–1197.

[34] C. Oezerdem et al., 16-channel bow tie antenna transceiver array for cardiac MR at 7.0 tesla, Magn. Reson. Med. 75 (6) (2016) 2553–2565.

[35] A.J.E. Raaijmakers, P.R. Luijten, C.A. van Den Berg, Dipole antennas for ultrahigh-field body imaging: a comparison with loop coils, NMR Biomed. 29 (9) (2016) 1122–1130.

[36] M.A. Ertürk et al., Toward imaging the body at 10.5 tesla, Magn. Reson. Med. 77 (1) (2017) 434–443.

[37] O. Ipek, A.J. Raaijmakers, D.W. Klomp, J.J. Lagendijk, P.R. Luijten, C.A. van den Berg, Characterization of transceive surface element designs for 7 tesla magnetic resonance imaging of the prostate: radiative antenna and microstrip, Phys Med. Biol. 57 (2) (2011) 343–355.

[38] M.A. Ertürk, A.J. Raaijmakers, G. Adriany, K. Uğurbil, G.J. Metzger, A 16-channel combined loop-dipole transceiver array for 7 T esla body MRI, Magn. Reson. Med. 77 (2) (2017) 884–894.

[39] B.R. Steensma et al., An 8-channel Tx/Rx dipole array combined with 16 Rx loops for high-resolution functional cardiac imaging at 7 T, Magn Reson Mater Phy 31 (1) (2018) 7–18.

[40] S.A. Aussenhofer, A.G. Webb, An eight-channel transmit/receive array of TE01 mode high permittivity ceramic resonators for human imaging at 7T, J. Magn Reson 243 (2014) 122–129.

[41] S.X. Xin, Q. Huang, Y. Gao, B. Li, Y. Xu, W. Chen, Fetus MRI at 7 T: shimming strategy and SAR safety implications, IEEE Trans. Microw. Theory Techn. 61 (5) (2013) 2146–2152.

[42] T.S. Ibrahim, Ultrahigh-field MRI whole-slice and localized RF field excitations using the same RF transmit array, IEEE Trans. Med. Imag. 25 (10) (2006) 1341–1347.

[43] W. Mao, M.B. Smith, C.M. Collins, Exploring the limits of RF shimming for high field MRI of the human head, Magn. Reson. Med. 56 (4) (2006) 918–922.

[44] C.M. Collins, W. Liu, B.J. Swift, M.B. Smith, Combination of optimized transmit arrays and some receive array reconstruction methods can yield homogeneous images at very high frequencies, Magn. Reson. Med. 54 (6) (2005) 1327–1332.

[45] H. Yoo, A. Gopinath, J.T. Vaughan, A method to localize RF field in high-field magnetic resonance imaging systems, IEEE Trans. Biomed. Eng. 59 (12) (2012) 3365–3371.

[46] I.A. Elabyad, T. Herrmann, C. Bruns, J. Bernarding, D. Erni, RF shimming and improved SAR safety for MRI at 7 T with combined eight-element stepped impedance resonators and traveling-wave antenna, IEEE Trans. Microw. Theory Techn. 66 (1) (2018) 540–555.

[47] I.A. Elabyad, M. Terekhov, M.R. Stefanescu, D. Lohr, M. Fischer, L.M. Schreiber, Design and evaluation of a novel symmetric multichannel transmit/receive coil array for cardiac MRI in pigs at 7 T, IEEE Trans. Microw. Theory Techn. http://doi:10.1109/TMTT.2019.2913636.

[48] A.L. Perrier et al., Design of a two-channel NMR coil using an impedance transformation approach, IEEE Sens. J. 12 (6) (2012) 1801–1808.

[49] M. Kozlov, R. Turner, Fast MRI coil analysis based on 3-D electromagnetic and RF circuit co-simulation, J. Magn Reson 200 (1) (2009) 147–152.

[50] T. Zhang, J.M. Pauly, S.S. Vasanawala, M. Lustig, Coil compression for accelerated imaging with Cartesian sampling, Magn. Reson. Med. 69 (2) (2013) 571–582.

[51] P. Vernickel et al., Eight-channel transmit/receive body MRI coil at 3T, Magn. Reson. Med. 58 (2) (2007) 381–389.

[52] M. Schmitt et al., A 128-channel receive-only cardiac coil for highly accelerated cardiac MRI at 3 Tesla, Magn. Reson. Med. 59 (6) (2008) 1431–1439.

[53] O. Weinberger et al., Local multi-channel RF surface coil versus body RF coil transmission for cardiac magnetic resonance at 3 Tesla: which configuration is winning the game?, PloS One 11 (9) (2016) 1–23